

Competing aggregation and iso-density equilibrium lead to band pattern formation in density gradients

Felix Maurer^{1*}, Camila Romero¹, Nikolas Lerch¹, Thomas John¹,
Lars Kaestner^{1,2}, Christian Wagner^{1,3}, Alexis Darras^{1*}

¹Experimental Physics, Saarland University, Campus, Saarbrücken,
66123, Saarland, Germany.

²Department of Theoretical Medicine and Biosciences, Saarland
University, Homburg, 66421, Saarland, Germany.

³Physics and Materials Science Research Unit, University of
Luxembourg, Luxembourg, L-4365, Luxembourg.

*Corresponding author(s). E-mail(s): mail@felixmilanmaurer.com;
alexis.charles.darras@gmail.com;

Abstract

Centrifugation of erythrocytes (aka Red Blood Cells, RBCs) in a self-forming Percoll gradient is a protocol often used as a way to sort RBCs by age. However, a pattern formation of discrete bands is systematically observed along the continuous density gradient. Although early studies mentioned that aggregation between cells might modify their spatial distribution, it is debated whether a population with continuous density distribution can form discrete bands. Here, we develop a continuity equation, considering the aggregation of cells with a continuous density distribution, which describes the macroscopic evolution of the RBC volume concentration in a density gradient. The numerical solutions demonstrate that the competition between iso-density distribution and aggregation is sufficient to create band patterns. Our model reproduces the temporal evolution observed in the conventional experimental protocol, but also predicts several types of bifurcation-like behaviors for the steady-state patterns in constant gradients, when the volume fraction and aggregation energy of the cells are varied. We therefore discovered that the competition between RBC aggregation and iso-density distribution is a novel physical mechanism leading to pattern formation.

Keywords: pattern formation, density separation, cell aggregation, red blood cells/erythrocytes

Research into density gradient media started in the 1960s and led to huge advances in the separation protocols of biological matter [1–12]. Density gradients are usually prepared through concentration gradients in suspensions of nanoparticles or macromolecular solutions, with different sedimentation dynamics than the biological objects to separate [1–5]. Among these media, suspensions of biocompatibly coated silica nanoparticles, known commercially as Percoll, have found extensive utility in the separation of Red Blood Cells (RBCs) [5–12]. Since the mass density of RBCs increases over their lifetime of approximately 120 days, density separation is considered a convenient way to separate RBCs according to their age [6, 7, 9]. During the past 40 years, several studies reported characteristic discontinuous RBC distributions of distinct bands, referred to as heterogeneous fractionation (see Fig. 1 (b,h)) [5–12]. The underlying mechanism was unknown, sometimes attributed to intrinsic cell characteristics, e.g., heterogeneous ion exchange or cytoskeleton configurations [11]. However, early observations of RBC redistribution after a second centrifugation indicated the presence of aggregation [6]. We previously identified cell aggregation as the most likely underlying mechanism in band pattern formation thanks to a series of experiments where the aggregability of RBCs was altered [13]. However, it was so far unclear how reproducible discrete band patterns could arise from a continuous distribution of RBC density through their aggregation.

Independently of RBC density separation methods, mechanics of pattern formation is a whole field of study on its own and is strongly related to biological systems, as it determines the morphogenesis of organisms [14–19]. Paradigmatic models for microscopic systems include Turing patterns (from reaction-diffusion) and diffusion-aggregation mechanisms [20–25]. Pattern formation, which is the result of a symmetry breaking, can also appear in more general dynamic instabilities, where two antagonistic processes compete for the dynamics of the system (e.g., Rayleigh-Bénard, Rayleigh-Taylor, and Benjamin-Feir instabilities) [26–28]. Recently, it has also been shown that dynamic density functional theory (DDFT) can also lead to pattern formation with repulsive interactions, or "social distancing", when modeling disease transmission in a population [29]. Among the possible patterns obtained in all these situations, band patterns are usually considered as the simplest ones, which can even appear in one-dimensional systems. However, their appearance and properties depend on the exact mechanisms and boundary conditions of the system in which they occur.

In this work, we present a continuum DDFT model that describes the macroscopic evolution of the distribution of RBCs in a Percoll gradient. It demonstrates that deterministic band patterns spontaneously form from the competition between iso-density equilibrium, i.e., buoyant forces, and intercellular aggregation forces. Therefore, we discovered a new physical mechanism that leads to pattern formation, which needs to be taken into account when studying cell density separation, as sometimes performed in clinical contexts [12].

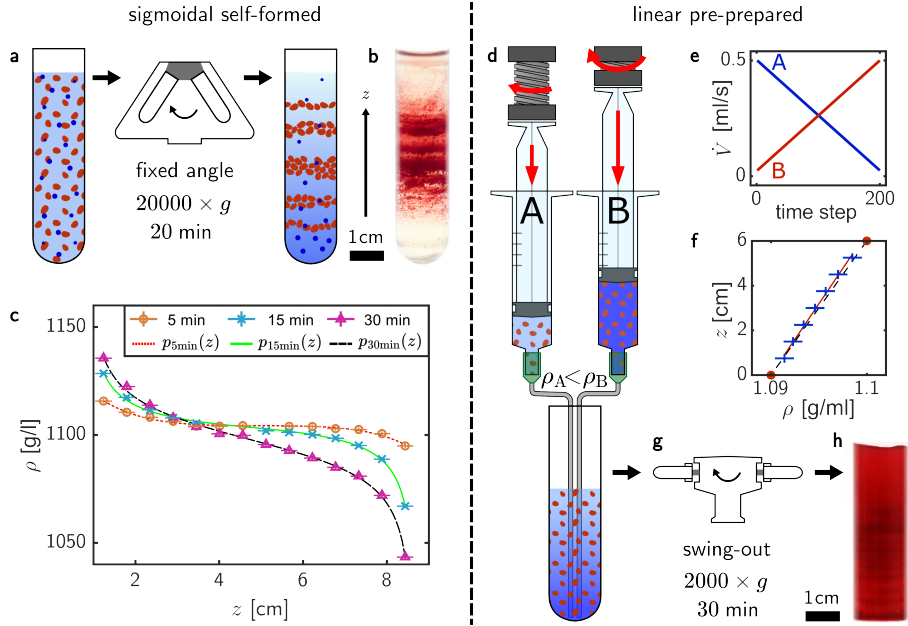


Fig. 1 Density gradient formation protocols and resulting band patterns. (Left side) Self-forming gradient. **a** Scheme of a standard separation protocol. RBCs are suspended in a Percoll medium matching the average cell density, with a hematocrit (i.e. average RBC volume fraction $\langle\psi\rangle$) of 2%. The tube is placed in a fixed-angle rotor. Percoll particles form a concentration gradient and RBCs arrange in bands. **b** Photograph of the resulting distribution. The z -axis coincides with the tube axis. **c** Measurements of a self-formed gradient for different centrifugation durations T_c . Colored markers are measurements, while curves are regressions of a sigmoidal function (Eq.(1)). (Right side) Prepared linear gradient **d** Syringe pump setup. Syringes A and B hold Percoll media of different densities $\rho_A < \rho_B$ and equal hematocrit $\langle\psi\rangle = 5\%$. The densities are chosen symmetrically around the average cell density. Pistons are driven by linear actuators at different speeds during 8 min in 200 steps. **e** The flow rate is changed linearly and inversely between A and B. **f** Measurement of a resulting linear gradient. Marker lines show error bars, red dots mark the starting densities. A linear regression (red line) is close to the expected gradient (broken line). **g** The gradient is placed in a swing-out rotor. **h** Photograph of the resulting RBC distribution in the tube, for $\langle\psi\rangle = 5\%$.

Protocols in biological or biochemical studies for the age separation make use of the spontaneous self-formation of a density gradient in Percoll, as described in Fig. 1a,b. Initially, a suspension of RBCs is either mixed with (or carefully placed on top of) a homogeneous Percoll medium in a centrifugation tube. The tube is then subjected to high accelerations $\geq 20000 \times g$ for a duration of 20 min. Nano-sized Percoll particles then experience partial sedimentation and adopt a sigmoidal density distribution. Control measurements of the density profiles without cells are shown in Fig. 1c. The density $p(z, t)$ of 14 layers extracted successively from the tube, 1 ml each, was measured using an Anton Paar Density Meter, see Fig. 1. Measurements were repeated for different duration of centrifugation t . An inverse sigmoidal function,

with time-dependent slope and curvature,

$$p(z, t) = p_0 + \delta(t) \frac{\chi}{(1 - |\chi|^{\mu(t)})^{\mu(t)-1}} \quad (1)$$

was fitted to obtain an analytical model for the purpose of simulation [2–4]. Further discussion of this choice is available in the Supplementary Material. The average density $p_0 = 1.1 \text{ g ml}^{-1}$ is assumed to be in the center of the centrifugation tube of length L . The density function has point symmetry with respect to the normalized coordinate $\chi = (z - z_0)\lambda^{-1}$, where λ is a characteristic length of the gradient. There is a time-dependent density spread $\delta(t) = \delta_1 t^{\delta_2}$, and steepness $\mu(t) = \mu_1 t + \mu_2$. All coefficients $(\lambda, \delta_1, \delta_2, \mu_1, \mu_2)$ were obtained from regressions to measured curves at various durations $t = T_c$.

When RBCs are added to the tubes during the formation of the Percoll concentration gradient, they are believed to drift towards their iso-density position, where buoyant force and external acceleration balance. This should result in a sorting by density. However, when resolved in a Percoll gradient, RBCs spatial distribution organizes into a pattern of discrete and separate bands [5–12, 30], see Fig. 1b. There is, however, no explanation why the mass density distribution of RBCs should be discrete and/or multimodal. In fact, for most applications, the distribution of the physiological RBC mass density can often be approximated as a Gaussian centered around 1.1 g ml^{-1} with a standard deviation of 4 mg ml^{-1} [31, 32].

Seeking a deeper explanation and mathematical description of the pattern formation process, we established a numerical model based on the assumption that the dynamics of the RBCs is only governed by the acceleration of the effective mass and aggregation. As demonstrated in the Supplementary Materials, the *DDFT*-equation for the specific volume fraction $\varphi(\rho, z, t)$ of RBCs of density ρ and volume V , at height z and time t can be written as

$$\zeta \partial_t \varphi = \frac{2\pi}{V} \partial_z \left(\varphi \int (z' - z) u(|z' - z|) \psi' dz' \right) - aV \partial_z (\varphi [\rho - p(z, t)]) , \quad \psi = \int \varphi d\rho , \quad (2)$$

where $\zeta = 8.97 \times 10^{-8} \text{ kg s}^{-1}$ is the Stokes drag coefficient of the RBCs with hydrodynamic radius $R = 2.8 \text{ }\mu\text{m}$, $u(|\mathbf{r} - \mathbf{r}'|)$ is the effective interaction potential between two RBCs located at \mathbf{r} and \mathbf{r}' , \mathbf{a} is the inertial acceleration due to the centrifugation process and $p(z, t)$ is the density of the surrounding Percoll suspension [33, 34]. By that definition, $\psi(\mathbf{r}, t)$ is the volume fraction of RBC at location \mathbf{r} . A common choice for the effective potential in case of short range interactions, like depletion, is the term $\exp(-r^n/\sigma^n)$. The effective potential combines attraction and repulsion,

$$u(r) = \frac{\mathcal{N}}{4\pi\sigma^3} \left(\frac{1 - \epsilon}{2} \frac{n_{\text{rep}}}{\Gamma\left(\frac{3}{n_{\text{rep}}}\right)} \exp\left(-\frac{r^{n_{\text{rep}}}}{\sigma^{n_{\text{rep}}}}\right) - \frac{1 + \epsilon}{2} \frac{n_{\text{att}}}{\Gamma\left(\frac{3}{n_{\text{att}}}\right)} \exp\left(-\frac{r^{n_{\text{att}}}}{\sigma^{n_{\text{att}}}}\right) \right) , \quad (3)$$

with the cell diameter σ , the attractiveness ϵ , and $-\mathcal{N}\epsilon = \int u(r)dV$ the amplitude of the interaction. We define an effective attractive energy U by $\mathcal{N} = UV_{\text{int}}\epsilon^{-1}$, $V_{\text{int}} = \frac{4}{3}\pi\sigma^3$. The numerical solver is implemented in C^{++} using CUDA, see supplementary section 2 and published code on *GitHub* [35]. Equation (2) was solved for $\sigma = 5.6 \mu\text{m}$, $n_{\text{att}} = 6$, $n_{\text{rep}} = 12$, i.e. in analogy to a typical Lennard-Jones potential. The initial condition was always homogeneous in space, which corresponds to mixing the sample tube, and a physiological distribution in density $\varphi(z, \rho, 0) = \langle \psi \rangle (2\pi\sigma_\rho^2)^{-\frac{1}{2}} e^{-(\rho - \langle \rho \rangle)^2 / 2\sigma_\rho^2}$ with $\langle \rho \rangle = 1.1 \text{ g ml}^{-1}$, $\sigma_\rho = 4 \text{ mg ml}^{-1}$. We solved the model for the traditional *sigmoidal self-forming* gradient as well as a new *stable linear* gradient separation protocol, in order to probe the properties of the obtained pattern in a simpler case. The effective energy was fixed to $U = 31.5 \text{ fJ}$ and $\langle \psi \rangle$ was varied.

The solution for the standard protocol, Fig. 1a, is depicted in Fig. 2. Experiments

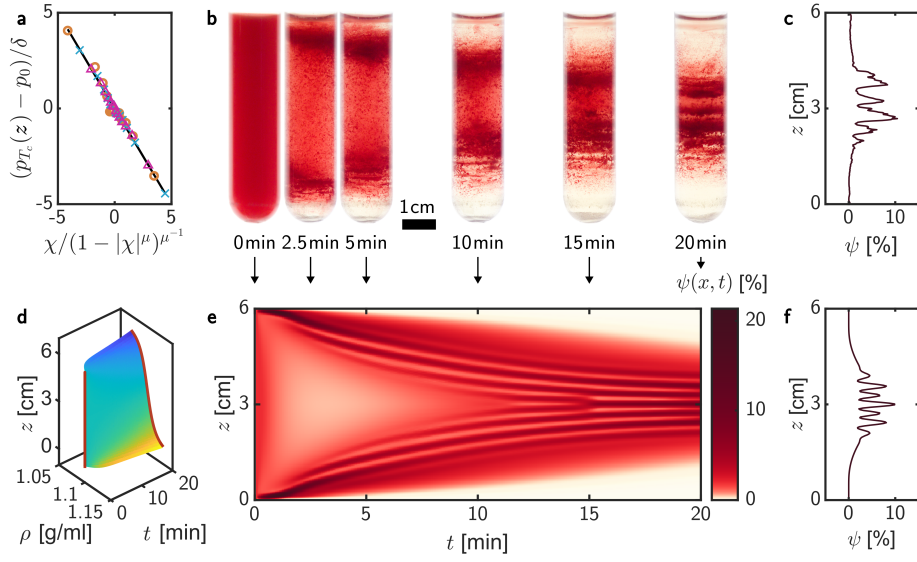


Fig. 2 Lab protocol for RBC fractionation in a self-forming gradient and simulation. **a** Collapse of measured sigmoidal density gradients after rescaling using the fit function (black line), Eq.(1). **b** Photographs from the separation protocol after different T_c . The sample hematocrit was 2%. **c** End state of the experiment showing distinct bands. $\psi(z)$ was obtained from image intensity profiles (see details in Supp. Mat.). **d** Gradient function adapted from regression to measurements, Eq.(1), with a linear spread. **e** Simulation of a similar system with $\langle \psi \rangle = 2\%$ for comparison. **f** End state of the simulation, showing distinct bands similar to the experiment.

were performed with average Percoll density matching the average RBC density [31, 32]. Images after different centrifugation duration are shown in Fig. 2b. Initially,

the Percoll density is constant as the medium is homogeneous, $p(z, t = 0) = p_0$. Consequently cells with a lower density than the surrounding medium, i.e. $\rho_{\text{RBC}} < p_0$, move to the top and remaining cells to the bottom. In case of perfect density matching and a symmetrical mass density distribution this divides the population exactly in half. After the gradient catches up, the sedimentation is accelerated by the formation of the density gradient. This causes an overall flow towards the center of the tube. During that process, band formation can be observed.

The gradient function $p(z, t)$ in Eq.(1) was adapted from regressions with $\lambda = 0.0338 \text{ m}$, $\delta_1 = 3.1773 \times 10^{-4} \text{ m}^3 \text{ kg}^{-1} \text{ s}^{-\delta_2}$, $\delta_2 = 1.52$, $\mu_1 = 1.1012 \times 10^{-3}$, and $\mu_2 = 0.6$. The system length is $L = 6 \text{ cm}$. The simulated RBC density is in good agreement with the experimentally observed distribution, Fig. 2e. This includes time scales, i.e., the initial split $t < 2 \text{ min}$, and the recombination with the development of a central band $t = 15 \text{ min}$, the number and amplitude of bands. Differences include the condensation of the distribution tails in the top and bottom of the tube due to xy heterogeneity, and uncontrollable variations in the experiment. Those variations might be induced by thermal or other convection, vibrations, and an offset in density matching.

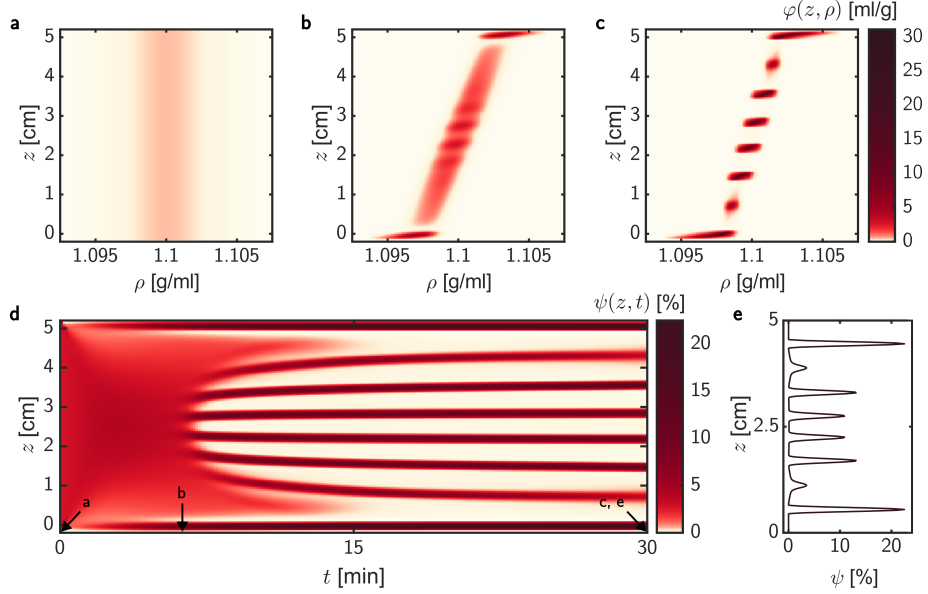


Fig. 3 Simulation results for sedimentation in a stable linear gradient at $\langle \psi \rangle = 2.8\%$. **a-c** RBC density function $\varphi(z, \rho, t)$ at different time points during simulation (0, 6.5 and 20 min, respectively). **a** and **c** respectively show the initial homogeneous and final state, while **b** depicts a time point near the onset of band formation. **d** Time evolution of the volume fraction $\psi(z, t)$. The distribution width is smallest at around 2 min, when of upward and downward moving cells are crossing around the middle of the sample. At $t \approx 6$ min distinct bands are forming which continue to sediment towards equilibrium. **e** symmetric end state showing three bands and tails near the borders.

In order to perform conceptually simplified experiments, we designed controllable Percoll concentration gradients, in order to study the final band pattern in various well-defined gradients and volume fractions. We used two computer-controlled syringe pumps to prepare a linear Percoll gradient and a homogeneous RBC distribution as shown in Figure 1d-f. Syringe A holds a low density medium with the desired hematocrit $\langle \psi \rangle$, and B a high density medium, $\rho_B > \rho_A$, with the same cell concentration. The needle tips are joined in the tube bottom to achieve mixing (Fig.1d). The volume flow is driven by linear actuators and varied to create a linear gradient (Fig.1e,f). Afterwards the sample is placed in a swing-out centrifuge at $2000 \times g$ for 30 min (Fig.1g). An example of resulting band pattern is depicted in Fig.1h. This method uses lower accelerations, so that the distribution of Percoll does not substantially changes during the sedimentation process. Hence it can be realized with a variety of affordable rotors, including more delicate swing-out variants. It is also more straightforward to implement corresponding numerical simulations, as the density gradient $p(z)$ can be considered stable along time with $\partial p / \partial z$ constant. Fig. 3 displays a typical time evolution obtained in the corresponding numerical simulation with a stable linear density gradient, while Fig. 4 compares experimental and numerical outcomes.

In a stable linear gradient, bands only appear above a critical concentration. Figure 4a shows the final cell distribution after centrifugation under the same conditions for different hematocrits $\langle\psi\rangle$. It reveals a complex branching behavior in which the number of bands might increase or decrease with increasing hematocrit. Figure 4c shows the simulation end state for different $\langle\psi\rangle$. The competition between buoyant forces and aggregation can therefore predict the emergence of various band patterns depending on the suspension properties and explains the high sensitivity of the band pattern on the experimental conditions.

In this study we proved that, when RBCs are placed in a density gradient, the

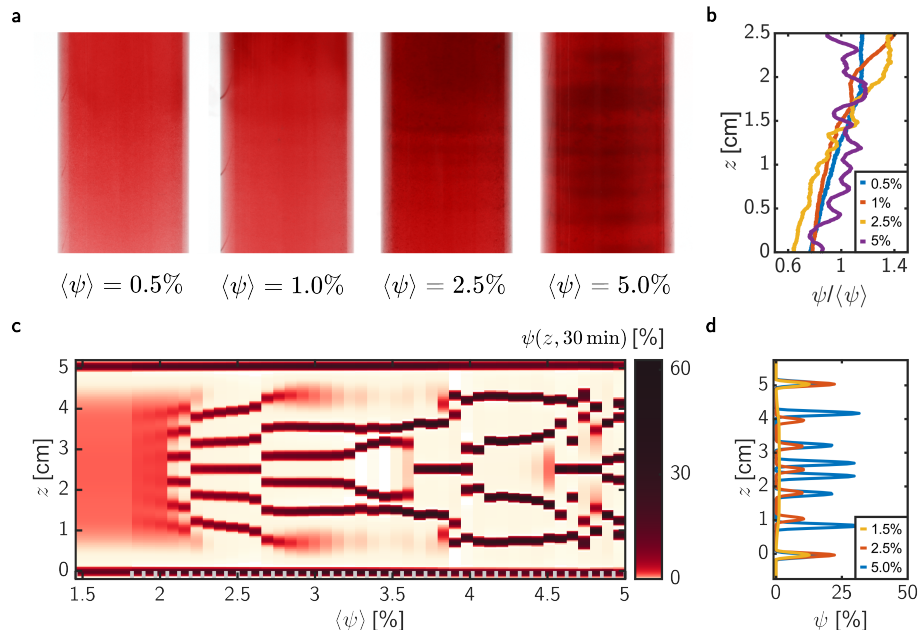


Fig. 4 Final band structures in linear gradients, for various hematocrits $\langle\psi\rangle$. **a** Experimental photographs for different hematocrits. **b** Extracted distribution of the volume fraction, based on the image intensity profiles. Bands appear starting from $\approx 2\%$ Ht. **c** Simulation end state for the same system size and different volume concentrations $\langle\psi\rangle$. There is a continuous emergence of a band pattern around 2% Ht. With increasing concentration there are various bifurcations between *even* solutions, and *odd* solutions with a central band. **d** Distributions of the volume fraction in numerical simulations, for selected values of $\langle\psi\rangle$.

assumption of an attractive pair interaction predicts band pattern formation in their spatial distribution, even if they have a monomodal and continuous mass density distribution. Our continuum model provides an explanation for the time evolution

during centrifugation and final state of the RBC density function. This opens perspective to model and predict properties of RBCs based on the observation of their band patterns, which has the potential of contributing to and enhance diagnostic predictions [12]. Moreover, preparing determined density gradients might allow to determine conditions to obtain more sensitive and/or more reproducible protocols to obtain pattern formations, which can now be explained theoretically. In summary, this band pattern formation process is a novel physical mechanism generating pattern formation with a complex bifurcation diagram, whose comprehension presents an exciting new challenge for researchers in the field of soft matter and biophysics, with potential clinical applications.

Author Contribution Statement

FM, TJ, LK, CW and AD developed the scientific question. FM, TJ, and AD designed the research study, and developed the initial model and solver. CW and AD obtained research funds. FM and TJ designed the experimental protocols. FM developed, performed and supervised experiments. FM wrote the final version of the model and its numerical solver, debugged, maintained and performed numerical simulations. CR investigated the time dependency of the self-forming gradient. CR and NL performed experiments. FM gathered and organized all results. FM and AD wrote the first version of the manuscript. All authors interpreted the results and wrote or reviewed the manuscript. All authors have read and agreed to the published version of the manuscript.

Acknowledgements

A.D. acknowledges funding by the Young Investigator Grant of the Saarland University. We gratefully acknowledge the computing time granted on the supercomputer MOGON II at JGU as part of NHR South-West (nhsw.de) [36].

1 Ethical statement

Human blood withdrawal from healthy volunteers was performed after explicitly obtaining their informed consent. Blood withdrawal and handling were performed according to the declaration of Helsinki and the approval by the ethics committee "Aerztekammer des Saarlandes" (reference No 176/21).

References

- [1] Mateyko, G.M., Kopac, M.J.: Part II: Isopyknotic Cushioning During High-Speed Centrifugation. *Annals of the New York Academy of Sciences* **105**(4), 219–285 (1996) <https://doi.org/10.1111/j.1749-6632.1963.tb42980.x>
- [2] Pertoft, H., Laurent, T.C.: Isopycnic Separation of Cells and Cell Organelles by Centrifugation in Modified Colloidal Silica Gradients. In: Catsimpoalas, N.

- (ed.) *Methods of Cell Separation*, pp. 25–65. Springer US, Boston, MA (1977). https://doi.org/10.1007/978-1-4684-0820-1_2
- [3] H. Pertoft, T.L. T. C. Laurent, Kagedal, L.: Density Gradients Prepared from Colloidal Silica Particles Coated by Polyvinylpyrrolidone (Percoll). *Analytical Biochemistry* **88**, 271–282 (1978) [https://doi.org/10.1016/0003-2697\(78\)90419-0](https://doi.org/10.1016/0003-2697(78)90419-0)
- [4] GE Healthcare: Cell Separation Media, Methodology and Applications. (2007). GE Healthcare. <https://www.lobov.com.ar/downloads/Handbook%20Cell%20Separation.PDF>
- [5] Vettore, L., De Matteis, M.C., Zampini, P.: A new density gradient system for the separation of human red blood cells. *American Journal of Hematology* **8**(3), 291–297 (1980) <https://doi.org/10.1002/ajh.2830080307>
- [6] Lutz, H.U., Stammli, P., Fasler, S., Ingold, M., Fehr, J.: Density separation of human red blood cells on self forming percoll gradients: Correlation with cell age. *Biochimica et Biophysica Acta (BBA) - General Subjects* **1116**(1), 1–10 (1992) [https://doi.org/10.1016/0304-4165\(92\)90120-J](https://doi.org/10.1016/0304-4165(92)90120-J)
- [7] Wesseling, M.C., Wagner-Britz, L., Huppert, H., Hanf, B., Hertz, L., Nguyen, D.B., Bernhardt, I.: Phosphatidylserine Exposure in Human Red Blood Cells Depending on Cell Age. *Cellular Physiology and Biochemistry* **38**(4), 1376–1390 (2016) <https://doi.org/10.1159/000443081>
- [8] Makhro, A., Kaestner, L., Bogdanova, A.: NMDA Receptor Activity in Circulating Red Blood Cells: Methods of Detection. In: Burnashev, N., Szepietowski, P. (eds.) *NMDA Receptors* vol. 1677, pp. 265–282. Springer New York, New York, NY (2017). https://doi.org/10.1007/978-1-4939-7321-7_15
- [9] Kämpf, S., Seiler, E., Bujok, J., Hofmann-Lehmann, R., Riond, B., Makhro, A., Bogdanova, A.: Aging Markers in Equine Red Blood Cells. *Frontiers in Physiology* **10**, 893 (2019) <https://doi.org/10.3389/fphys.2019.00893>
- [10] Huisjes, R., Makhro, A., Llaudet-Planas, E., Hertz, L., Petkova-Kirova, P., Verhagen, L.P., Pignatelli, S., Rab, M.A.E., Schiffelers, R.M., Seiler, E., van Solinge, W.W., Corrons, J.-L.V., Kaestner, L., Mañú-Pereira, M., Bogdanova, A., van Wijk, R.: Density, heterogeneity and deformability of red cells as markers of clinical severity in hereditary spherocytosis. *Haematologica* **105**(2), 338–347 (2020) <https://doi.org/10.3324/haematol.2018.188151>
- [11] Bogdanova, A., Kaestner, L., Simionato, G., Wickrema, A., Makhro, A.: Heterogeneity of Red Blood Cells: Causes and Consequences. *Frontiers in Physiology* **11**, 392 (2020) <https://doi.org/10.3389/fphys.2020.00392>
- [12] Sadafi, A., Makhro, A., Livshits, L., Navab, N., Bogdanova, A., Albarqouni, S., Marr, C.: Sick Cell Disease Severity Prediction from Percoll Gradient

Images using Graph Convolutional Networks (2021) <https://doi.org/10.48550/arXiv.2109.05372> [arXiv:2109.05372](https://arxiv.org/abs/2109.05372)

- [13] Maurer, F., John, T., Makhro, A., Bogdanova, A., Minetti, G., Wagner, C., Kaestner, L.: Continuous Percoll Gradient Centrifugation of Erythrocytes—Explanation of Cellular Bands and Compromised Age Separation. *Cells* **11**(8), 1296 (2022) <https://doi.org/10.3390/cells11081296>
- [14] Ben Amar, M., Ciarletta, P., Haas, P.A.: Morphogenesis in space offers challenges and opportunities for soft matter and biophysics. *Communications Physics* **6**(1), 150 (2023) <https://doi.org/10.1038/s42005-023-01242-9>
- [15] Cross, M.C., Hohenberg, P.C.: Pattern formation outside of equilibrium. *Reviews of modern physics* **65**(3), 851 (1993) <https://doi.org/10.1103/RevModPhys.65.851>
- [16] Newman, S.A., Comper, W.D.: ‘generic’physical mechanisms of morphogenesis and pattern formation. *Development* **110**(1), 1–18 (1990) <https://doi.org/10.1242/dev.110.1.1>
- [17] Davies, J.A., Glykofrydis, F.: Engineering pattern formation and morphogenesis. *Biochemical Society Transactions* **48**(3), 1177–1185 (2020) <https://doi.org/10.1042/BST20200013>
- [18] Tsai, T.Y.-C., Sikora, M., Xia, P., Colak-Champollion, T., Knaut, H., Heisenberg, C.-P., Megason, S.G.: An adhesion code ensures robust pattern formation during tissue morphogenesis. *Science* **370**(6512), 113–116 (2020) <https://doi.org/10.1126/science.aba6637>
- [19] Sudderick, Z.R., Glover, J.D.: Periodic pattern formation during embryonic development. *Biochemical Society Transactions* **52**(1), 75–88 (2024) <https://doi.org/10.1042/BST20230197>
- [20] Gao, S., Chang, L., Perc, M., Wang, Z.: Turing patterns in simplicial complexes. *Physical Review E* **107**(1), 014216 (2023) <https://doi.org/10.1103/PhysRevE.107.014216>
- [21] Turing, A.M.: The chemical basis of morphogenesis. *Bulletin of mathematical biology* **52**, 153–197 (1990) <https://doi.org/10.1007/BF02459572>
- [22] Katz, L., Silva-Dias, L., Dolnik, M.: Turing patterns in the chlorine dioxide-iodine-malonic acid reaction–diffusion batch system. *Journal of Chemical Education* (2024) <https://doi.org/10.1021/acs.jchemed.3c01208>
- [23] Bengfort, M., Malchow, H., Hilker, F.M.: The fokker–planck law of diffusion and pattern formation in heterogeneous environments. *Journal of mathematical biology* **73**, 683–704 (2016) <https://doi.org/10.1007/s00285-016-0966-8>

- [24] Carrillo, J.A., Craig, K., Yao, Y.: Aggregation-diffusion equations: dynamics, asymptotics, and singular limits. *Active Particles, Volume 2: Advances in Theory, Models, and Applications*, 65–108 (2019) <https://doi.org/10.48550/arXiv.1810.03634>
- [25] Fagioli, S., Radici, E.: Solutions to aggregation–diffusion equations with nonlinear mobility constructed via a deterministic particle approximation. *Mathematical Models and Methods in Applied Sciences* **28**(09), 1801–1829 (2018) <https://doi.org/10.48550/arXiv.1801.10114>
- [26] Charru, F.: *Hydrodynamic instabilities*. Cambridge Texts in Applied Mathematics **37** (2011) <https://doi.org/10.1017/CBO9780511975172>
- [27] Ecke, R.E.: Chaos, patterns, coherent structures, and turbulence: Reflections on nonlinear science. *Chaos: An Interdisciplinary Journal of Nonlinear Science* **25**(9) (2015) <https://doi.org/10.1063/1.4915623>
- [28] De Wit, A.: Chemo-hydrodynamic patterns and instabilities. *Annual Review of Fluid Mechanics* **52**, 531–555 (2020) <https://doi.org/10.1146/annurev-fluid-010719-060349>
- [29] Te Vrugt, M., Bickmann, J., Wittkowski, R.: Effects of social distancing and isolation on epidemic spreading modeled via dynamical density functional theory. *Nature communications* **11**(1), 5576 (2020) <https://doi.org/10.1038/s41467-020-19024-0>
- [30] Bogdanova, A., Kaestner, L.: Early career scientists’ guide to the red blood cell—don’t panic! *Frontiers in physiology* **11**, 588 (2020)
- [31] Weems, H.B., Lessin, L.S.: Erythrocyte Density Distribution in Sickle Cell Anemia. *Acta Haematologica* **71**(6), 361–370 (1984) <https://doi.org/10.1159/000206620>
- [32] Lew, V.L., Bookchin, R.M.: Ion Transport Pathology in the Mechanism of Sickle Cell Dehydration. *Physiological Reviews* **85**(1), 179–200 (2005) <https://doi.org/10.1152/physrev.00052.2003>
- [33] Royall, C.P., Dzubiella, J., Schmidt, M., Van Blaaderen, A.: Nonequilibrium Sedimentation of Colloids on the Particle Scale. *Physical Review Letters* **98**(18), 188304 (2007) <https://doi.org/10.1103/PhysRevLett.98.188304>
- [34] Dzubiella, J., Likos, C.N.: Mean-field dynamical density functional theory. *Journal of Physics: Condensed Matter* **15**(6), 147–154 (2003) <https://doi.org/10.1088/0953-8984/15/6/102>
- [35] Maurer, F.: NVCC implementation of Red Blood Cell pattern formation in a density gradient during sedimentation. <https://github.com/FelixMaurer/>

RedPatterns

- [36] Mainz, J.G.U.: NHR Süd-West. <https://hpc.uni-mainz.de/category/nhr-sued-west/>

Competing aggregation and iso-density equilibrium lead to band patterns in density gradients: Supplementary Material

Felix Maurer^{1*}, Camila Romero¹, Nikolas Lerch¹, Thomas John¹,
Lars Kaestner^{1,2}, Christian Wagner^{1,3}, Alexis Darras^{1*}

¹Experimental Physics, Saarland University, Campus, Saarbrücken,
66123, Saarland, Germany.

²Department of Theoretical Medicine and Biosciences, Saarland
University, Homburg, 66421, Saarland, Germany.

³Physics and Materials Science Research Unit, University of
Luxembourg, Luxembourg, L-4365, Luxembourg.

*Corresponding author(s). E-mail(s): mail@felixmilanmaurer.com;
alexis.charles.darras@gmail.com;

1 Establishment of the *DDFT*-equation

The number of RBCs per unit volume and mass density interval at location \mathbf{r} and time t is given by the density function $n(\mathbf{r}, \rho, t) d^3r d\rho$. We will use this section of the Supplementary Materials to derive the equations exploited in the main text.

1.1 Simplified physical explanation

This section offers a simplified justification of the equations we used. Although less rigorous than the next one, it is also easier to comprehend for non-experts.

The sedimentation force acting on a single cell of volume V and density ρ , in a surrounding liquid of density $p(z, t)$, is the effective buoyant force $\mathbf{f}_{\text{sed}} = \mathbf{a}V(\rho - p(z, t))$, taking into account a constant inertial acceleration \mathbf{a} due to the centrifugation of the sample. Given a drag coefficient of ζ , the associated flux reads

$$\mathbf{j}_{\text{sed}}(\mathbf{r}, \rho, t) = n(\mathbf{r}, \rho, t)\zeta^{-1}\mathbf{a}V(\rho - p(z, t)) . \quad (1)$$

A pair-interaction between cells leads to a flux

$$\mathbf{j}_{\text{int}}(\mathbf{r}, \rho, t) = \zeta^{-1} n(\mathbf{r}, \rho, t) \nabla_{\mathbf{r}} \iint n(\mathbf{r}', \rho', t) u(|\mathbf{r}' - \mathbf{r}|) d^3 r' d\rho', \quad (2)$$

where $u(|\mathbf{r}' - \mathbf{r}|)$ is the effective *mean-field* pair interaction potential between RBCs. Due to conservation of the number of RBCs, the density function is assumed to fulfill a continuity equation.

$$\partial_t n(\mathbf{r}, \rho, t) = -\nabla_{\mathbf{r}} \cdot \mathbf{j}(\mathbf{r}, \rho, t), \quad \mathbf{j} = \mathbf{j}_{\text{sed}} + \mathbf{j}_{\text{int}} \quad (3)$$

1.2 General *DDFT*-equation

One can also rigorously derive the previous partial differential equation from the *DDFT*-equation

$$\frac{\partial n(\mathbf{r}, \rho, t)}{\partial t} = \zeta^{-1} \nabla_{\mathbf{r}} \cdot \left(n(\mathbf{r}, \rho, t) \nabla_{\mathbf{r}} \left(\frac{\delta F[n]}{\delta n(\mathbf{r}, \rho, t)} \right) \right) \quad (4)$$

where $F[n]$ is the intrinsic Helmholtz free energy functional and ζ^{-1} is the mobility. In general there are three contributions to F , the energy of an ideal gas F_{id} , the excess energy over an ideal gas F_{exc} , and the contribution from an external potential F_{ext} [1]. The free energy of the ideal gas F_{id} is irrelevant for our athermal system. The excess free energy however originates in the interactions between particles. A good estimation for a one-component system of soft particles is given by the *mean-field* or *random-phase approximation* [2].

$$F_{\text{exc}}[n] = \frac{1}{2} \int d^3 r d^3 r' d\rho d\rho' u(|\mathbf{r} - \mathbf{r}'|) n(\mathbf{r}, \rho, t) n(\mathbf{r}', \rho', t), \quad (5)$$

where $u(r)$ is the effective pair interaction potential between RBCs. The external term is given by the external potential $u_{\text{ext}}(\mathbf{r}, t)$,

$$F_{\text{ext}}[n(\mathbf{r}, \rho, t)] = \int d\rho \int d^3 r n(\mathbf{r}, \rho, t) u_{\text{ext}}(\mathbf{r}, t). \quad (6)$$

The potential associated with the net-acceleration during sedimentation is $u_{\text{ext}}(\mathbf{r}, t) = -\mathbf{r} \cdot \mathbf{a} V(\rho - P(\mathbf{r}, t))$, with \mathbf{a} the inertial acceleration due to the centrifugation process, V the volume of a cell and $P(\mathbf{r}, t)$ the density of the surrounding fluid (i.e. the Percoll suspension). Finally, for this system the *DDFT* equation then reads

$$\zeta \partial_t n = \nabla_{\mathbf{r}} \cdot \left(\frac{n}{2} \nabla_{\mathbf{r}} \int d^3 r' d\rho' u(|\mathbf{r} - \mathbf{r}'|) n(\mathbf{r}', \rho', t) \right) + \nabla_{\mathbf{r}} \cdot (n \nabla_{\mathbf{r}} u_{\text{ext}}(\mathbf{r}, t)) \quad (7)$$

For the specific system there are simplifications due to symmetry that reduce the problem to two dimensions. The density function is assumed to be constant in the

plane orthogonal to the centrifugal acceleration \mathbf{a} . In cylindrical coordinates, with $\mathbf{a} = |\mathbf{a}|\mathbf{e}_z$, the equation reads

$$\zeta \partial_t n = \partial_z \left(2\pi n \int dz' d\rho' (z' - z) u(|z' - z|) n(z', \rho', t) \right) - aV \partial_z (n(\rho - p(z, t))) , \quad (8)$$

for a one-dimensional gradient $p(\mathbf{r}, t) = p(z, t)$, and where $n = n(z, \rho, t)$.

For an easier comparison with experimental results, it is practical to work with the specific volume fraction $\varphi(\mathbf{r}, \rho, t) = Vn(\mathbf{r}, \rho, t)$,

$$\zeta \partial_t \varphi = \frac{2\pi}{V} \partial_z \left(\varphi \int dz' (z' - z) u(|z' - z|) \psi' \right) - aV \partial_z (\varphi(\rho - p(z, t))) , \psi = \int d\rho \varphi . \quad (9)$$

By that definition, $\psi(\mathbf{r}, t)$ is the volume fraction of RBC at location \mathbf{r} . This is then the equation that we solve numerically, as explained in the main text.

2 Numerical implementation

This section provides a summary of the most important considerations of the solver implementation.

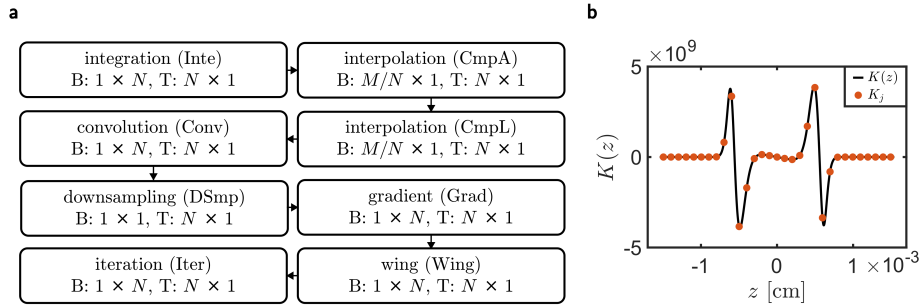


Fig. S1 **a** Flow chart of CUDA kernels, brackets show abbreviations. Each kernel has its own layout in the two-dimensional grid, i.e. number of Blocks (B) and number of Threads per Block (T). **b** Continuous kernel function $K(z)$ and the sampled vector K_j used in numerical calculations. Parameters are $n_{\text{att}} = 6$, $n_{\text{rep}} = 12$, $\epsilon = 8 \times 10^{-7}$.

2.1 Grid and units

We work with a grid with size $N \times N = 2^k \times 2^k$. In all presented solutions it is $k = 8 \Rightarrow N = 256$. The coordinate arrays are the spatial z_i and mass density ρ_j discrete values. Discrete versions of density functions are φ_{ij} and ψ_i . We work with $\phi_{ij} \equiv \Delta\rho \varphi_{ij}$, s.t. we can use the approximation $\psi_i = \sum_j \phi_{ij}$. Both quantities, ψ_i and ϕ_{ij} are dimensionless.

2.2 Operators

The time differential ∂_t is approximated with first order forward differences with increment Δt , spatial derivatives ∂_z by first order central differences, denoted by D_z , with increment Δz . The interaction integral is represented by a discrete convolution with the kernel array K_j , $j = 1, \dots, 2m + 1$, $m \in \mathbb{N}_0$ with an uneven number of elements, $K_j = \frac{2\pi}{\mathcal{N}} z_j u(z_j)$. The kernel is depicted in **S1b**. Since the energy is integral normalized, the sampled kernel K_j is normalized. The deviation to the exact integral needs to be taken into account in the attractivity ϵ . This is implemented by a correction $\epsilon \rightarrow \epsilon + \xi$, s.t. $\sum_j u(z_j)/\mathcal{N} = \epsilon$ is true again. Parameters were fixed to $\epsilon = 8 \times 10^{-7}$, $\xi = -3.1 \times 10^{-3}$.

2.3 Discrete continuity equation

The continuity equation for the grid $N \times N$ reads

$$-\Delta t^{-1}(\phi_{ij}^{t+1} - \phi_{ij}^t) = \frac{aV}{\zeta} D_z [\phi_{ij}^t (\rho_j - p_i^t)] - \frac{\mathcal{N}}{\zeta V} D_z \left[\phi_{ij}^t \sum_{l=1}^{2m+1} \psi_{i+l-m-1}^t K_l \Delta z \right].$$

For performance reasons the continuity equation is solved on a coarser scale L/N with the stability condition that the width of RBC bands is larger than the resolution of the coarse grid, but the kernel integration is computed on a finer grid M , $w_{\text{band}} \gg L/N > w_{\text{kernel}} \gg L/M$. In all the displayed solutions, it is $M = 256N = 65536$. The volume fraction ψ_i is interpolated, the interaction term is calculated and finally sampled down. The upsampling is a standard cubic spline interpolation and the downsampling a simple point-wise evaluation. The numerically solved equation can then finally be written

$$-\Delta t^{-1}(\phi_{ij}^{t+1} - \phi_{ij}^t) = \frac{aV}{\zeta} D_z [\phi_{ij}^t (\rho_j - p_i^t)] - \frac{\mathcal{N}}{\zeta V} D_z [\phi_{ij}^t I_i^t],$$

$$I_i = \left[\sum_{l=1}^{2m+1} \psi_{i+l-m-1}^{\text{upsmp},t} K_l \Delta z \frac{\mathcal{N}}{M} \right]^{\text{downsmp}}.$$

2.4 Restrictions

The RBC volume fraction is restricted to $0 \leq \phi_{ij}$ and $0 \leq \psi_i \leq 1$. Those restrictions are implemented using degenerate diffusion terms. Consequently negative amplitudes due to numerical noise are prevented increasing stability of the solver. The degenerate diffusion terms are $\gamma D_z^2 \left(1 - \left(\frac{\phi_{ij}}{\langle \psi \rangle} \right)^{m_{\text{deg}}} \right)$ and $\delta D_z^2 \left(\frac{\psi_i}{\langle \psi \rangle} \right)^{m_{\text{deg}}}$ with empirical values for the exponent $m_{\text{deg}} = 500$ and $\iota = 0.05$. The scaling factors $\gamma, \delta \approx 10^{-10}$ are chosen to guarantee the restriction without influencing the dynamics, i.e. the resulting pattern.

2.5 Explicit scheme

With all terms included, we get the iterative scheme for the time step $t \rightarrow t + 1$.

$$\begin{aligned} \phi_{ij}^{t+1} = & \phi_{ij}^t - \Delta t \left(\alpha D_z [\phi_{ij}^t (\rho_j - p_i^t)] - \beta D_z [\phi_{ij}^t I_i^t] + \gamma D_z^2 \left(1 - \left(\frac{\phi_{ij}^t}{\langle \psi \rangle} \right)^{m_{\text{deg}}} \right) \right. \\ & \left. - \delta D_z^2 \left(\frac{\psi_i^t}{\langle \psi \rangle} \right)^{m_{\text{deg}}} \right) \end{aligned}$$

with $\alpha = \frac{aV}{\zeta}$, $\beta = \frac{N}{\zeta V}$.

2.6 CUDA kernels

The computations during a time step are divided into different kernels, see Fig. S1a. Each kernel runs on a two-dimensional grid (blocks $B : B_x \times B_y$, threads per block $T : T_x \times T_y$) tailored to optimize efficiency. The first kernel integrates to obtain ψ_i . The latter is then sampled up using a standard cubic spline interpolation with natural spline boundary conditions. The interpolation is split into two kernels (CmpA, CmpL). The purpose of CmpA is the computation of

$$\alpha[i] = 3(\psi[i+1] - \psi[i]) - 3(\psi[i] - \psi[i-1]) \quad (10)$$

and CmpL takes care of the iterative scheme.

$$\begin{aligned} \mu[i] &= \frac{1}{4 - \mu[i-1]} \\ z[i] &= \frac{\alpha[i] - z[i-1]}{4 - \mu[i-1]} \\ \mu[j] &= \frac{1}{4 - \mu[j+1]} \\ c[j] &= z[j] - \mu[j]c[j+1] \\ b[j] &= y[j+1] - y[j] - \frac{c[j+1] + 2c[j]}{3} \\ d[j] &= \frac{c[j+1] - c[j]}{3} \\ l[k] &= \psi[j] + (b[j] + (c[j] + d[j]\Delta z)\Delta z)\Delta z. \end{aligned}$$

The interpolated values are obtained directly as $\psi_k^{\text{upsmpl}} = l[k]$. This is followed by the convolution kernel (Conv) and the downsampling kernel (Dsmpl), that evaluates I at the coarse N grid points. The gradient kernel (Grad) computes the Percoll density function $p(z, t)$ for the given time step into a device array. System boundaries are implemented in form of wings extending the gradient (Wing). Finally the iteration kernel (Iter) computes flux terms, flux derivatives with first order central differences, and executes an Euler step of $\varphi_{i,j}$.

3 Density gradient modeling

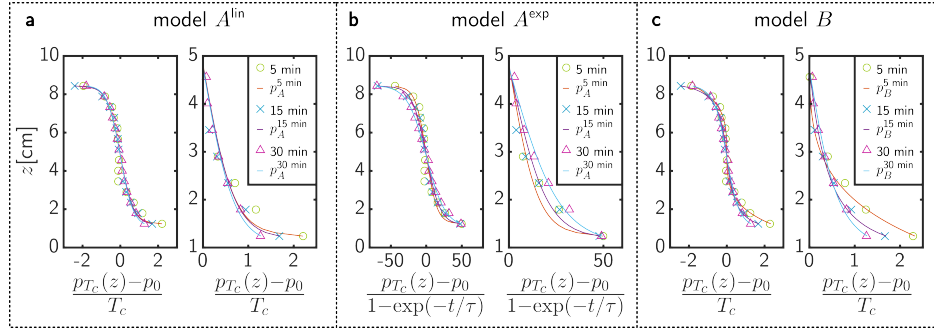


Fig. S2 Data collapse; comparison of different models. **a** Model A^{lin} from Eqn. 12 assumes a linear scaling with time, but does not sufficiently reproduce the time dependent curvature. Tails of the density distribution show a divergence between experimental measurements and fitted curves. **b** Model A^{exp} from Eqn. 13, with $\tau = 20$ min, produces a collapse of the tails only. **c** Model B following Eqn. 15 describes both the collapse near the center as well as the tails correctly.

In this section the time development of the Percoll density function $p(z, t)$ is discussed. Maurer et al. [3] previously suggested a fit model to the measured data of centrifugation duration T_c ,

$$p_A^{T_c}(z) = b_1 + b_2^{T_c} \log \left(\frac{b_4}{x - b_3} - 1 \right), \quad (11)$$

with free parameters b_i . The scaling parameter b_2 is assumed to depend on T_c . After fitting the model to measurements, assumptions have to be made for the time dependency of the parameter $b_2(t)$ in order to obtain a continuous equation for $p(z, t)$. Two variations of this model (A) is here compared to the model (B) introduced in the main article. Indeed, a closer look at the measured data and different model assumptions (A^{lin} , A^{exp} , B) justify the choice of a more elaborate mathematical equation in the numerical simulations of this article.

Laurent et al. reported a linear increase of the slope in the symmetry center of the gradient with time [4]. The first assumption A^{lin} is therefore a linear scaling with t as given by $b_2(t) = at$, and introducing constants with a notation consistent with physical quantities, one can write

$$p(z, t) = p_0 + \log \left(\frac{\lambda}{z - z_0} - 1 \right) \times at. \quad (12)$$

While the fitted curves (A), displayed in Fig. S2a, are consistent with the experimental data near the center, there is no change in curvature towards the tails. The measurements however suggest that this curvature decreases with time. For their particle

model, Maurer et al. [3] described the gradient with $b_2(t) = \epsilon(1 - \exp(-t/\tau))$,

$$p(z, t) = p_0 + \log\left(\frac{\lambda}{z - z_0} - 1\right) \times \epsilon(1 - \exp(-t/\tau)), \quad (13)$$

This assumption manages to describe the scaling of the tail, however the linear scaling near the center is lost, see Fig. S2b.

The updated fit function in this article is given by

$$p_A^{T_c}(z) = b_1 + b_2^{T_c} \frac{\chi(z)}{\left(1 - |\chi(z)|^{b_5^{T_c}}\right)^{1/b_5^{T_c}}}, \quad \chi(z) = \frac{z - b_3}{b_4}. \quad (14)$$

The fitted curves (Fig. S2c) correctly describe both the linear collapse near the center and the change of tail curvature. The final model

$$p(z, t) = p_0 + \delta(t) \frac{\chi}{\left(1 - |\chi|^{\mu(t)}\right)^{\mu(t)^{-1}}} \quad (15)$$

then assumes the dependencies $\delta(t) = \delta_1 t^{\delta_2}$ and $\mu(t) = \mu_1 + \mu_2 t$ leading to the complete collapse shown in the article (Fig. 2a).

4 Imaging color model

This section details how RGB values from the experimental photographs have been calibrated to corresponding hematocrit values. The same color scale has been used to depicts the volume fraction $\psi(z, t)$ obtained from numerical simulations, in order to allow a direct visual comparison.

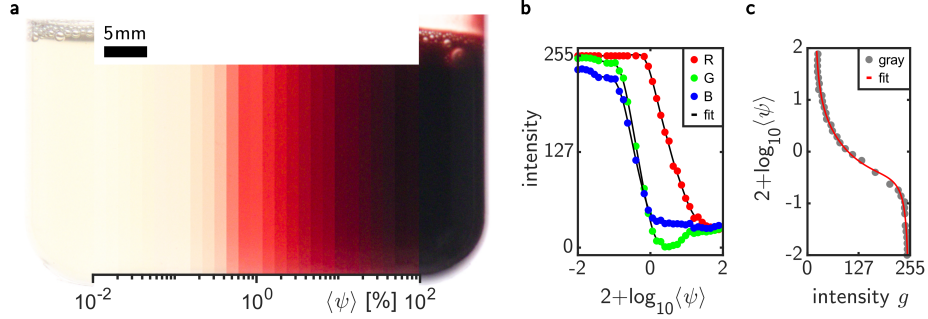


Fig. S3 RBC concentration to RGB value conversion. **a** Experimental photographs of 31 different RBC concentrations in isotonic Percoll solution. **b** Smoothing spline fit to each color channel. Dots mark average intensity values from a region of interest in the center of each sample tube, black lines show splines. **c** inverse conversion model from grayscale intensity to RBC concentration. Dots are average values of the color channels, the red line shows a regression of the model Eqn. 16.

A total of 31 solutions of hematocrits on a logarithmic scale ranging from 10^{-2} to 10^2 % were prepared. RBCs were suspended in isotonic Percoll solution to account for the interaction of light with all constituents. Each suspension was filled in the same tube used for density gradient centrifugation, and *RAW* photographs were taken under the same lighting conditions with a *Canon M50* mirrorless digital camera with the EF-M 18-150 mm zoom lens at 150 mm, aperture $f/8$, and shutter $1/60$ s. Tonemapping from raw *CR3* format to RGB was performed using *RawTherapee* (rawtherapee.com), see attached *.pp3* file for detailed parameters. The image series is shown in Fig. S3a. For each photograph, a mask was drawn by hand to select a center region of each tube. The RGB channels were averaged over that area and plotted as a function of the logarithmic volume fraction in percent, $2 + \log_{10}\langle\psi\rangle$. A smoothing spline was fitted to the 8-bit intensity values (0, ..., 255) of each channel using the *fit* function in *Matlab*, see Fig. S3b. The resulting regression curves were used to obtain RBC triplets from the simulated $\psi(z, t)$. The gray values g , i.e. the average intensity value of the color channels, were plotted versus the volume fraction $\langle\psi\rangle$ and the sigmoidal function

$$\psi^{\log}(g) = b_1 + b_2 \frac{\frac{g-b_3}{b_4}}{\left(1 - \left(\frac{g-b_3}{b_4}\right)^{b_5}\right)^{-1}} + b_6(g - b_3)^2, \quad \psi = 10^{\psi^{\log}} \%, \quad (16)$$

was fitted, see Fig. S3c. The resulting parameters were $b_1 = -0.022$, $b_2 = -0.062$, $b_3 = 134.8$, $b_4 = 118.2$, $b_5 = 2.004$, $b_6 = 2.95 \times 10^{-5}$. This calibration is then later used in order to extract the local volume fraction $\psi(z, t)$ from the experimental pictures.

References

- [1] Royall, C.P., Dzubiella, J., Schmidt, M., Van Blaaderen, A.: Nonequilibrium Sedimentation of Colloids on the Particle Scale. *Physical Review Letters* **98**(18), 188304 (2007) <https://doi.org/10.1103/PhysRevLett.98.188304>
- [2] Dzubiella, J., Likos, C.N.: Mean-field dynamical density functional theory. *Journal of Physics: Condensed Matter* **15**(6), 147–154 (2003) <https://doi.org/10.1088/0953-8984/15/6/102>
- [3] Maurer, F., John, T., Makhro, A., Bogdanova, A., Minetti, G., Wagner, C., Kaestner, L.: Continuous Percoll Gradient Centrifugation of Erythrocytes—Explanation of Cellular Bands and Compromised Age Separation. *Cells* **11**(8), 1296 (2022) <https://doi.org/10.3390/cells11081296>
- [4] H. Pertoft, T.L. T. C. Laurent, Kagedal, L.: Density Gradients Prepared from Colloidal Silica Particles Coated by Polyvinylpyrrolidone (Percoll). *Analytical Biochemistry* **88**, 271–282 (1978) [https://doi.org/10.1016/0003-2697\(78\)90419-0](https://doi.org/10.1016/0003-2697(78)90419-0)